CRYSTAL GROWTH & DESIGN

Article

Cite This: *Cryst. Growth Des.* 2019, 19, 6752−6762

pubs.acs.org/crystal

Insight into the Interfacial Nucleation and Competitive Growth of $YBa_2Cu_3O_{7-\delta}$ Films as High-Performance Coated Conductors by a Fluorine-Free Metal−Organic Decomposition Route

Jingyuan Chu,[†] Yue Zhao,[*,†,‡] Mukarram Z. Khan,[§] Xiao Tang,[∥] Wei Wu,[†] Jiangtao Shi,[†] Yue Wu,[†] Hannu Huhtinen,[§] Hongli Suo,[⊥] and Zhijian Jin[†]

[†]School of Electronic Information and Electrical Engineering, Shanghai Jiao Tong University, 200240 Shanghai, People's Republic of China

[‡]Shanghai Superconductor Technology Co., Ltd., 200240 Shanghai, People's Republic of China

[§]Wihuri Physical Laboratory, Department of Physics and Astronomy, University of Turku, Turku 20014, Finland

[∥]King Abdullah University of Science and Technology (KAUST), Advanced Semiconductor Laboratory, Thuwal 23955-6900, Saudi Arabia

[⊥]College of Materials Science and Engineering, Beijing University of Technology, 100022 Beijing, People's Republic of China

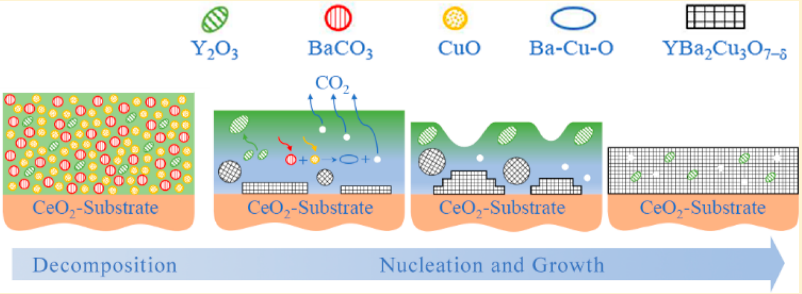

ABSTRACT: The fluorine-free metal−organic decomposition (FF-MOD) route is one of the table-top methods for the growth of high-quality superconducting $YBa_2Cu_3O_{7-\delta}$ (YBCO) films due to its advantages of being environmentally friendly and having a faster film deposition rate. However, the nucleation and growth mechanism originated during this process are not yet comprehensively understood. In this paper, the microstructural characteristics of YBCO films quenched from different growth stages were investigated, upon which a complete nucleation and growth model is established. A micro-Raman and scanning electron microscopy (SEM) coordinated study demonstrates the coexistence of polycrystalline and epitaxial grains at the early stage of nucleation. Combined analysis of transmission electron microscopy (TEM) and secondary ion mass spectroscopy (SIMS) indicates that YBCO epitaxial nucleates by following the Volmer−Weber growth mode. We observed that as the growth process proceeds, the nuclei at the interface have a significant growth advantage over those in the body, thus leading to coalescence of island epitaxial grains via consuming neighboring polycrystalline grains and intermediate phases. Moreover, by establishing a kinetic phase diagram of YBCO film growth, we also found that the optimal process conditions are mainly related to the enhanced transient liquid phase and $BaCeO_3$, which are somehow associated with the cross-linkage between the sintering temperature, dwell time, and oxygen partial pressure (pO_2) of the sintering atmosphere. Remarkably, a high critical current density (J_c) value of 3.6 MA/cm^2 (77 K, self-field) was obtained in the YBCO film grown on the CeO_2 capped technical substrate deposited under optimized conditions, which is rather comparable with that on the $LaAlO_3$ single crystal. The angular-dependent J_c analysis revealed that the anisotropy of the YBCO film is reduced to 3, as estimated by the Blatter scaling approach, which is much smaller than that of the typical defect-free pristine films. This work improves understanding of the nucleation and growth mechanism in the YBCO film deposited on the CeO_2-buffered technical substrate and facilitates the industrialization development of epitaxial oxide films with superior performance in the future.

1. INTRODUCTION

The second-generation high-temperature superconducting tapes (2G HTS) based on $REBa_2Cu_3O_{7-\delta}$ films (REBCO, where RE is Y or rare earth element) have attracted a great deal of attention in various practical application such as power transmission cables, electronic devices, and superconducting magnets.[1−3] Deposition of REBCO films is mainly categorized into in situ and ex-situ methods. In the former, the REBCO phase is formed directly just after the deposition process, such as in pulsed laser deposition (PLD) and metal−organic

Received: August 22, 2019
Revised: October 2, 2019
Published: October 16, 2019

DOI: 10.1021/acs.cgd.9b01120
Cryst. Growth Des. 2019, 19, 6752−6762

chemical vapor deposition (MOCVD) methods, whereas in the latter the deposition and phase formation processes (sometimes also called coating and heat treatments respectively) are carried out separately, that is, in processes such as reactive coevaporation (RCE) and metalorganic decomposition (MOD).

Because of different phase formation mechanisms, each technique results in distinguished microstructure characteristics that lead to different superconducting properties. To date, many researchers have carried out extensive studies on the nucleation and growth of YBCO films.[4−7] Usually, the YBCO films grown by in situ techniques follow the Stranski−Krastanov growth mode,[8,9] which gives us the columnar type structural growth. This results in the fact that the microstructure (especially the grain boundary networks) of YBCO films highly inherits that in the underlying substrate.[10] In the case of ex-situ processes, especially MOD routes, a laminar structure is formed, and the crystallographic alignment of YBCO is improved compared with that of the template, which leads to a significant reduction of grain boundaries with large misorientation angles. Such a phenomenon is explained by the overgrowth mechanism due to liquid-phase mediated laminar grain growth.[11]

Up to now, both the in situ and ex-situ deposition techniques have been adopted by 2G tape manufacturers worldwide, and great progresses have been achieved. Among them, MOD is considered as one of the most cost-effective and suitable techniques for YBCO deposition. Because no vacuum apparatus (low investment cost) is needed, precise composition/stoichiometry control and scalability for industrial production can be achieved by this route.[12,13] Depending on the presence of fluorine in the precursors, MOD routes can also be categorized into trifluoroacetate metal organic decomposition (all TFA-MOD or low TFA-MOD) and fluorine-free (FF-MOD) routes. The TFA-MOD process has been extensively studied, and high J_c coated conductors have also been manufactured worldwide.[14,15] In this process, YBCO films nucleate following a Volmer−Weber mode. Namely, island-like YBCO grains first form at preferred nucleation sites at the interface, and then the growth front smoothly moves to the film surface with the harmful gases (HF) diffusion. Eventually, the grains coalesce, and a continuous dense film is formed.[16,17] The FF-MOD route naturally offers the possibility of fast pyrolysis and higher growth rate without the generation of HF gases.[18,19] However, more knowledge of the FF-MOD route focuses on how to get rid of the harmful intermediate phase $BaCO_3$ based on the solid-state reaction mechanism.[20,21] A clear picture of interfacial nucleation and the 3D growth model is essential in terms of further improvement of the superconductivity. Moreover, mapping the effect of processing parameters on the microstructure is required for the sake of industrialization.

In our previous works, we proposed a simple and novel FF-MOD precursor solution, by which high-quality YBCO films were successfully grown on $LaAlO_3$ single crystals and CeO_2 capped technical substrates.[22,23] Herein, we aim to give deeper insight into the correlation between the microstructure and superconductivity in the FF-MOD YBCO films, and finally the epitaxial growth model for YBCO on the CeO_2 capped technical substrate has been established. J_c (θ, H) of the YBCO films were comprehensively studied by using Quantum Design physical property measurement system (PPMS). Specimens quenched at each stage of the growth process were characterized by means of X-ray diffraction (XRD), atomic force microscopy (AFM), SEM, dynamic SIMS, TEM, energy dispersive spectrometer (EDS), and micro-Raman spectroscopy. On the basis of our results, we built up a complete kinetic phase diagram where the effects of sintering temperature, pO_2, and dwell time on the film microstructures were clarified.

2. EXPERIMENTAL SECTION

2.1. Solution Synthesis and Growth of YBCO Films. YBCO films with approximately 200 nm of thicknesses were deposited by the FF-MOD route. The synthesis of propionate-based precursor solutions and heat-treatment of the YBCO films are reported elsewhere.[24] Textured metallic tapes with a configuration of CeO_2/$LaMnO_3$/IBAD-MgO/Y_2O_3/Al_2O_3/C276 (supplied by Shanghai Superconductor Technology) were used as substrates.[25] The fwhm values of CeO_2 (002) rocking curve and that of the CeO_2 (111) ϕ-scan are 2° and 3−4° respectively, being an indication of high texture quality. Prior to coating, the CeO_2 buffer tapes were cleaned sequentially in acetone and ethanol ultrasonic baths. The precursor solutions were dip coated with a withdrawal speed of 1 mm/s, which gave us the typical film thicknesses of around 200 nm after the full reaction. To complete the YBCO phase conversion, a typical three-step heat treatment process including pyrolysis, sintering, and oxygenation was performed in an atmosphere-controlled tubular furnace. The details of the procedure are described in ref 23. To investigate the nucleation and growth behavior of YBCO films, this study only focused on the sintering process. A set of specimens were prepared under different pO_2, dwell times and sintering temperatures.

2.2. Characterization of YBCO Film Structure and Superconducting Properties. Phase purity and crystallographic texture of the YBCO films were characterized by using four-circle XRD provided by Bruker D8 Advance and equipped with a two-dimensional detector with Cu−Kα radiation (λ = 1.54 Å). YBCO (103) and (005) reflections were used to evaluate the in-plane and out-of-plane texture quality, respectively. Morphology of the film surface was analyzed by SEM (Zeiss Auriga, equipped with an in-lens detector) and AFM (Bruker Multimode 8). A confocal Raman imaging system integrated in the SEM (RISE) was used to collect two-dimensional arrays of Raman spectra.[26] This technique enables investigation of the correlation between the surface morphology and chemical compound information in the same submicron areas observed by SEM (MAIA3, TESCAN). Micro-Raman measurements (WITec) were made with 532 nm wavelength incident laser light. The incident laser power was carefully tuned to avoid sample damage, and measurements were thus performed at around 8 mW incident laser power.

Cross-sectional TEM specimens were prepared by the focused ion beam technique with Ga^+ ion milling (FIB Zeiss Auriga). TEM imaging together with selected-area electron diffraction (SAED) and energy dispersive X-ray spectroscopy (EDX) studies were performed using an aberration-corrected scanning transmission electron microscope (STEM, JEOL ARM 200CF) with a double-tilt holder and a cold field emission source operated at 200 kV.

Elements distribution through the film thickness were verified by a dynamic SIMS instrument from Hiden Analytical Company (Warrington, UK) operated at 10^{-9} Torr. A continuous Ar^+ beam of 3 keV energy was applied to sputter the surface, while the selected ions were sequentially collected by using a MAXIM spectrometer equipped with a quadrupole analyzer.

J_c values at magnetic field perpendicular to the film surface were calculated from the hysteresis loops ($M-H$ curve) by using the Bean model:[27]

$$J_c = 2\Delta m/[a(1 - a/3b)V] \quad (1)$$

where a and b ($b \geq a$) are the width and the length of the specimen, V is the specimen volume, and Δm is the opening of the hysteresis loop, which is measured by PPMS at 77 K.

J_c (θ, H) curves at 50 K were obtained under applied magnetic fields μ_0H ranging from 0 to 8 T where samples were rotated from 0−360° (with θ = 0° for $H//c$ and 90° for $H//ab$), thus providing a detailed picture of pinning effects. For this purpose, the films were patterned by wet chemical etching with 200 μm wide current stripes.[28] The results under 50 K condition are more informative for comparison with other superconducting thin films.

3. RESULTS AND DISCUSSION

3.1. Superconductivity Properties of FF-MOD Derived YBCO Films. Nucleation and growth of YBCO films are mainly related to the enhanced transient liquid phase and interfacial reaction, which are somehow controlled by the cross-linkage between the sintering temperature and pO_2. Under optimized process windows (e.g., 760−810 °C and 50−100 ppm), a YBCO film with relatively pure phase is obtained on the CeO_2 capped technical substrate.[23] The inset of Figure 1 shows a schematic cross-section of our template used for growing films.

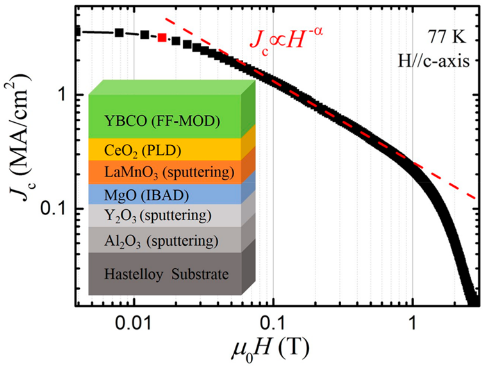

Figure 1. Log−log scale J_c (B) dependence ($H//c$) at 77 K for the FF-MOD YBCO film deposited on CeO_2 capped technical substrate, while the inset shows the full structure.

A YBCO film prepared under optimal growth conditions (e.g., 780 °C, 50 ppm, and a sintering dwell time of 90 min) was investigated by means of XRD as shown in Figure 2. The XRD θ-2θ scan (Figure 2a) shows predominant c-axis growth, as evidenced by strong (00l) peaks, the absence of (200) peaks, and negligible (013)/(103) peaks. The quantitative texture analysis (Figure 2b) reveals that the fwhm values of the ϕ-scan on CeO_2 (111) and that of the ϕ-scan on YBCO (103) are 3.2° and 2.4° respectively, being an indication of improvement in the in-plane texture in the YBCO film compared with that of the CeO_2 layer. This feature is mainly due to the overgrowth mechanism related to existence of the liquid phase.[10,19] Namely, the YBCO nuclei on well-oriented CeO_2 grains have growth advantages. With the proceeding of heat treatment, the YBCO with poor texture and polycrystalline grains are consumed by a grain growth process.

In order to understand the electromagnetic properties, the J_c (B) at 77 K and J_c (θ, H) at 50 K were measured on the YBCO film. First, log−log scale J_c (B) dependence (H//c at 77 K) in the YBCO film is plotted, as shown in Figure 1. Remarkably, a high J_c value of 3.6 MA/cm^2 was achieved on the CeO_2-buffered technical substrate at 77 K self-field, which is quite comparable with that grown on the $LaAlO_3$ single crystal.[29] It is known that accommodation field (B^*), defined as J_c (B^*) = 0.9*J_c(0), is normally associated with a single-pinning regime in the low field, while the parameter α in $J_c \propto B^{-\alpha}$ corresponds to a collective interaction regime of vortices in the medium fields range. In this film, it is calculated that B^* is 16 mT and α is about 0.67, which indicates that the flux pinning mechanisms are dominated by random and isotropic pinning on the film.[30]

Inset of Figure 3 shows $J_c(\theta)$ of the YBCO film at 50 K under different applied magnetic fields (from 0.5 to 8 T). It is notable that when the magnetic field H is parallel to the ab-planes, pronounced J_c peaks are observed at all the magnetic fields. This can be explained by intrinsic anisotropy of the YBCO, which is attributed basically not only to the pinning of vortices by the Cu−O planes but also to other extrinsic linear

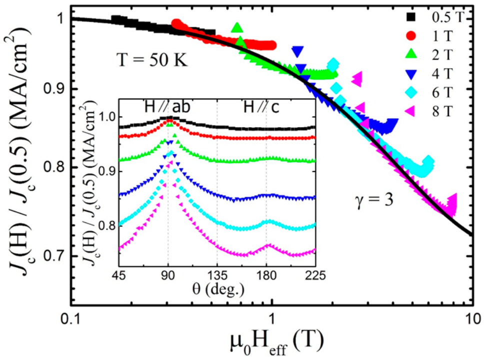

Figure 3. Log−linear plot of the J_c (θ, H) divided with the maximum values at 0.5 T as a function of the applied magnetic fields along the c-axis of YBCO film measured at 50 K. The solid (black) line represents the isotropic J_c contribution. The inset shows the J_c (θ) also measured at 50 K under different fields.

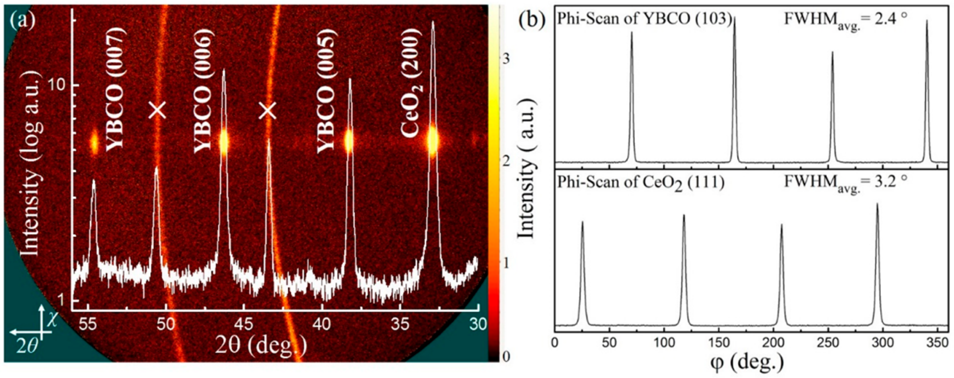

Figure 2. (a) Two-dimensional XRD frame of the YBCO film deposited on the CeO_2 substrate under optimal growth conditions (e.g., 780 °C, 50 ppm, and 90 min), where a typical θ-2θ plot is superposed. (b) XRD ϕ-scan of YBCO (103) (top) and CeO_2 (111) (bottom).

DOI: 10.1021/acs.cgd.9b01120
Cryst. Growth Des. 2019, 19, 6752−6762

or planar defects lying parallel to the *ab*-planes like stacking faults.[31,32] In addition, when the applied magnetic field is close to the *c*-axis direction, broad and weak peaks are also observed at high magnetic fields (e. g., 6 and 8 T), which is attributed to anisotropic pinning centers aligned with the *c*-direction, probably threading dislocations or a small amount of twin grain boundaries.[33,34] Obviously, the peak in the *c*-axis direction is much weaker than that parallel to the *ab*-planes in our case. It is because of no strong *c*-axis correlated defect observed in the XRD scans.

In order to shed more light on the J_c anisotropy behaviors of the YBCO film, the Blatter scaling approach is applied to analyze the $J_c(\theta, H)$ results.[35] The regions where J_c collapses were plotted as a function of the effective magnetic field, $H_{eff} = H\varepsilon(\gamma,\theta)$. Its expression is given as follows, and γ was defined as the anisotropy parameter:

$$\varepsilon^2(\gamma, \theta) = \cos^2(\theta) + \gamma^{-2} \sin^2(\theta) \qquad (2)$$

It is well-known that the larger the γ value, the more pronounced the film anisotropy. A smooth fitting curve, J_c^{iso} versus H_{eff}, was obtained with the γ value of 3 (Figure 3). This value is smaller than that of the typical defect-free pristine film prepared by either PLD[33] or MOD methods (γ = 5−7).[36] Since no artificial pinning center is introduced on purpose, the smaller anisotropy is probably related to a certain amount of uncorrelated defects, such as the high density of short stacking faults, Y_2O_3 nanoprecipitations and pores after the gas release, etc.[37]

3.2. Growth Kinetics of YBCO Films. According to the thermodynamic stability diagram of YBCO established by R. H. Hammond, it is known that the formation region of YBCO with a strong *c*-orientation is mainly dominated by the growth temperature and pO_2.[38] The phase diagrams are plotted under equilibrium conditions; however, other variables are not considered. In order to comprehensively study the YBCO film growth kinetics, a series of specimens were obtained by quenching from the sintering temperature and pO_2 at a dwell time of 0, 20, 40, 60, 90, 120, 140, 160, and 180 min, respectively. The overall phase and microstructure evolution from nucleation to the over-reaction is involved in this case. From the previous studies, it is known that the interface reaction trend occurs under a high sintering temperature, while *a*/*b*-axis orientation is easily predominated under a low sintering temperature and high pO_2. Therefore, a sintering condition of 780 °C and 50 ppm pO_2 is chosen as the initial point in this set of experiments. In addition, such low sintering temperature slows down the entire reaction process, which provides better conditions to separate/study each phase during the whole reaction.

XRD phase analysis was carried out to get a first insight into the phase evolution, focusing on two representative phases, YBCO and $BaCeO_3$. Integrated intensities of the YBCO (103) and (006), $BaCeO_3$ (110) peaks as a function of dwell time are plotted in Figure 4. It is found that only the YBCO (103) peak clearly appears at the initial stage, while no other phase was observed. With proceeding of the sintering, the YBCO (006) and $BaCeO_3$ (110) peaks gradually appeared. According to the evolution of these three phase components, we divide the whole process into three stages. It should be noted that there are no obvious boundaries in the three stages; i.e., the end of one stage is always accompanied by the beginning of the next stage. The first stage is up to 60 min, i.e., the initial strong *c*-axis orientated nucleation. At this stage, the YBCO (103) peak intensity gradually decreases, while the YBCO (006) peak gradually becomes stronger with the increase of the reaction time. This result indicates that the body nucleation already occurs and predominates prior to approaching the target sintering temperature, even under a relatively high heat ramping rate of 20 °C/min. In addition, we noticed that at the dwell time of 40 min, the YBCO (006) peak intensity increases slowly, but the YBCO (103) peak gradually weakens, indicating that the interface nucleation gradually dominates. The second stage is roughly from 60 to 120 min, i.e., the *c*-axis textured grain growth and coarsening stage. The YBCO (103) peak progressively reduces to a negligible level, whereas the integrated intensity of the YBCO (006) peak increases dramatically and reaches a plateau. It indicates that the nuclei at the interface have a growth advantage over those in the body. In addition, we did not observe any $BaCeO_3$ phase in the first two stages, suggesting that the interface reaction has not yet been triggered at these conditions. The third stage is roughly from 120 to 180 min, i.e., the interface reaction dominated stage. No YBCO (103) peak is discerned, but the $BaCeO_3$ (110) peak becomes pronounced, and the peak intensity rapidly increases with prolonging of the dwell time, being indicative of serious interfacial reactions. On the other hand, the intensity of the YBCO (006) peak intensity starts to decrease until it almost disappears.

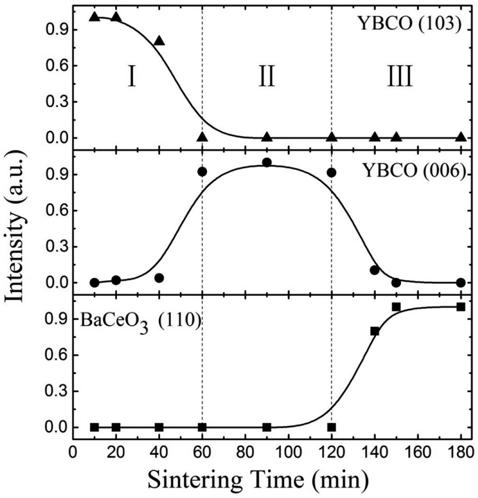

Figure 4. X-ray diffraction analysis on the specimens sintered at a different sintering time with a fixed sintering temperature of 780 °C and pO_2 of 50 ppm: integrated intensities of the YBCO (103) (top), YBCO (006) (middle), and $BaCeO_3$ (200) (bottom) peaks as a function of sintering time.

To establish the full picture of each stage, three representative samples were selected and investigated by using SEM and two-dimensional XRD. As shown in Figure 5a, at the initial strong *c*-axis orientated nucleation stage (e.g., the one quenched at 40 min), two types of microstructure features were observed. One is irregular-shaped regions at about 1 μm in diameter, consisting of plate-like grains with a smooth surface and embedded with some voids. The other is dense nanosized grains with a rough surface. AFM analysis indicates that the latter are about 70−100 nm lower than the irregular-shaped regions. Moreover, we noticed the presence of broad YBCO (103) diffraction ring and weak YBCO (200) and (00*l*) spots in the 2D XRD pattern (as shown in Figure 5d). It is a typical feature of random orientation nucleation, i.e.,

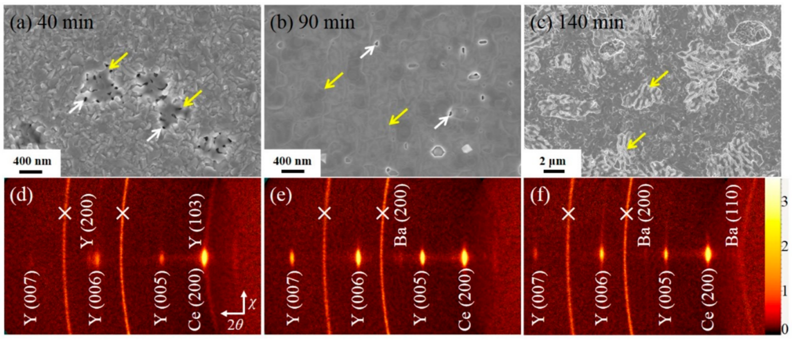

Figure 5. SEM images (a−c) and two-dimensional XRD frames (d−f) on the specimens sintered at different sintering times (stage) with a fixed sintering temperature of 780 °C and pO_2 of 50 ppm: (a, d) at 40 min, irregular-shaped regions surrounded by inclined nanosized grains pointed by yellow arrows and voids pointed by white arrows; (b, e) at 90 min, the meandering grain boundaries pointed by yellow arrows and pinholes pointed by white arrows; (c, f) at 140 min, dendrites pointed by yellow arrows. In the XRD frames, the Y, Ce, Ba, and cross symbols represent the diffractions from the YBCO, CeO_2, $BaCeO_3$, and the metallic substrate, respectively.

body nucleation, *a*-axis oriental nucleation, and *c*-axis nucleation competing with each other, which is principally attributable to a large enough Gibbs energy barrier (ΔG^*).[39] More detailed structural information on this region will be discussed in the following section.

At the grain orientation growth dominated stage (as shown in Figure 5b, e.g., the one quenched at 90 min), almost all the nanosized grains disappeared. Instead, a smooth dense surface with meandering grain boundaries is present on the film. Small amounts of pinholes are also seen, which is probably due to the densification during grain growth and coarsening. These are the common features for the YBCO films driven by the liquid assisted growth mechanism.[20,24] The dramatic changes in morphology are highly in agreement with the XRD results. As shown in Figure 5e, neither secondary phases nor the YBCO (103) peak is discerned in the 2D XRD pattern. Instead, only narrow YBCO (00*l*) spots were detected, revealing that the large plate-like grains correspond to the YBCO (00*l*) diffractions very well (i.e., strong *c*-axis orientation). In addition, weak $BaCeO_3$ (200) spot can be observed, which indicates that the interface reaction has already been started.

At the interface reaction dominated stage (as shown in Figure 5c, e.g., the one quenched at 140 min), the microstructure turns to in-homogeneous, i.e., dendritic segregations approximately 5−10 μm in length embedded in the dense and smooth matrix. EDS elemental distribution analysis indicates that these dendrites are Y-rich and Ba, Cu-poor (close to the Y_2BaCuO_5 phase) compared with the neighbor matrix. According to the 2D XRD analysis (as shown in Figure 5f), we noticed broad a $BaCeO_3$ (110) and (200) ring and YBCO (00*l*) spots broadening along the χ direction. This result reveals that the formation of a large amount of randomly orientated $BaCeO_3$ grains and deterioration of a well-orientated YBCO film. Such microstructure is the consequence of partial decomposition of the YBCO phase probably triggered by the enhanced liquid phase reacted with the CeO_2 cap-layer.

According to the aforementioned discussion, we established the correlation between the morphology and phase in the YBCO film from the aspect of growth kinetics under 780 °C and 50 ppm. It is well-known that the sintering temperature plays a very important role in the kinetics of YBCO nucleation and growth.[40] Therefore, in order to fully map the effect of sintering temperatures on the growth of YBCO film, a set of specimens were prepared under a sintering temperature ranging from 760 to 820 °C with a fixed pO_2. In order to give an overall picture of the whole process, the phase diagram of sintering temperature, dwell time, and phase composition was established (under a fixed pO_2 of 50 and 200 ppm, respectively), as shown in Figure 6.

In Figure 6a, we found that a YBCO film undergoes three typical stages of nucleation, growth, and interfacial reaction over the dwell time at all sintering temperatures. However, as

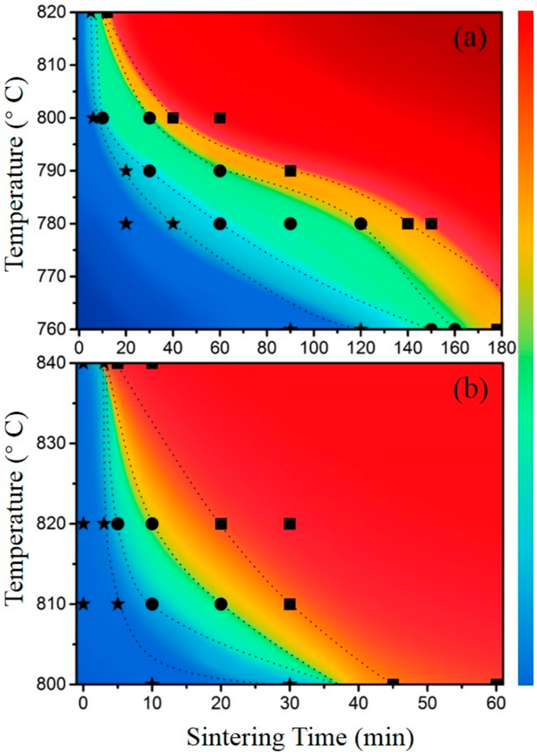

Figure 6. Phases diagram showing the effect of sintering time and temperature on YBCO formation during different reaction stages with a fixed pO_2 of 50 ppm (a) and 200 ppm (b). Note: The blue region represents the YBCO (103) phase (the asterisk depicts the initial strong *c*-axis orientated nucleation stage); the green region represents the well-oriented YBCO (the circle depicts the *c*-axis grain growth and coarsening stage); the red region reveals $BaCeO_3$ (the square depicts interface reaction dominated stage). The color intensity is for the amount of the corresponding phase.

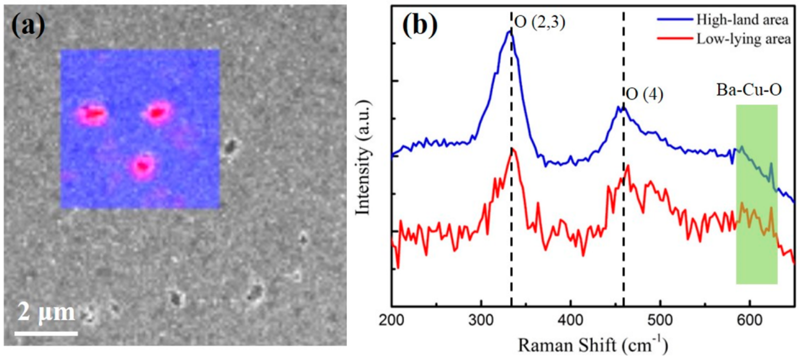

Figure 7. (a) RISE image of the region indicating high-land areas (blue) and low-lying areas (red). (b) Raman spectra extracted from cluster analysis for high-land area (blue) and low-lying area (red).

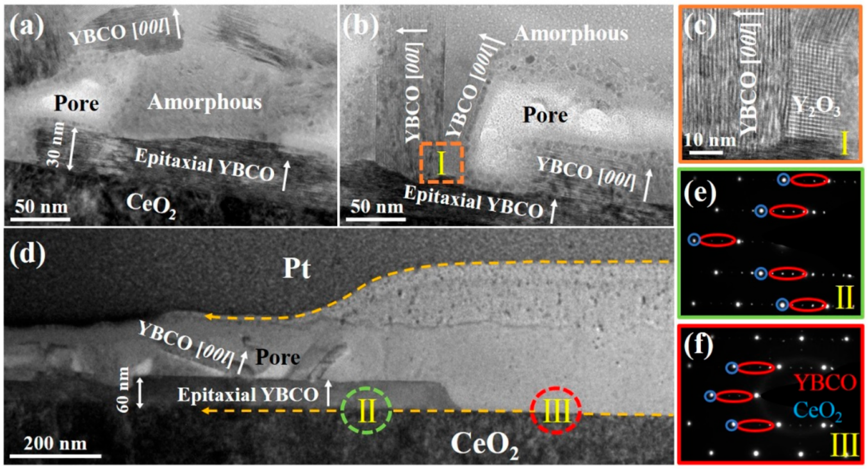

Figure 8. (a, b) Low-magnification TEM images of two high-land areas. (c) Zoom-in on the YBCO growth front at the frame I (orange) in (b). (d) Cross-sectional TEM images of a low-lying area. (e, f) SAED pattern at the interface between the YBCO layer and CeO_2 substrate at the frame II (green) and the frame III (red) in (d).

the sintering temperature decreases, each stage turns out to be prolonged, while the transition from one stage to the following one is delayed. It is because the higher the sintering temperature, the faster the elemental diffusion, which accelerates both the formation of the liquid phase and the occurrence of interfacial reactions. Meanwhile, the optimal growth condition window of the YBCO film is broadened at 780 °C as compared with other higher or lower sintering temperatures. This is also consistent with the results of our experimental reproducibility. Let us say, at a higher sintering temperature, the window of optimal sintering time is narrow, and the experimental reproducibility is low due to the rapid reaction. In some cases, it can be found that different stages of the regions coexist even in a film.

To study the effect of pO_2 on the nucleation and growth of the film, we also draw the phase diagram under a pO_2 of 200 ppm. Compared with the 50 ppm phase diagram, three main differences were observed in Figure 6b. First, although the three-stage regions still exist, the geometry is changed. Second, the optimal sintering temperature shifts to a higher temperature under 200 ppm conditions. For example, it is difficult to obtain a well-oriented YBCO film at 800 °C, even applying a longer dwell time. Third, the dwell time window at an optimized temperature becomes narrower; e.g., the broadest window of dwell time is shortened to 10 min at 200 ppm, compared with 60 min at 50 ppm (760 °C). It is suggested that choosing a lower pO_2 is more beneficial to precisely control the nucleation and growth stages of YBCO films, which results in optimal quality for industrial production by using the FF-MOD route.

In summary, the growth of FF-MOD YBCO films always undergoes three stages on the CeO_2 capped technical substrate, including (1) a initial strong *c*-axis orientated nucleation, (2) *c*-axis grain growth, and (3) coarsening stage. Furthermore, the timing for each stage is dominated by the nucleation thermodynamics and elemental diffusion.

3.3. Nucleation and Growth Mechanism of FF-MOD Derived YBCO Film.

In order to study the nucleation and growth mechanism of the FF-MOD derived YBCO films, a representative specimen quenched at the first stage (i.e., the initial strong *c*-axis orientated nucleation) was chosen for a detailed TEM investigation. Additional attention is paid to the nonuniform microstructure characteristics as displayed in Figure 5a. Two different topographical features appear: one is called high-land areas (i.e., inclined small grains), and the other is called low-lying areas (i.e., plated-like large grains with pin-holes), and the latter are about 70−100 nm lower than the surroundings. To understand the detailed structural information, we performed a micro-Raman and SEM coordinated study as well as HRTEM analysis on these two typical regions.

Figure 7 shows the micro-Raman mapping image superposed on the SEM picture on a region where these two

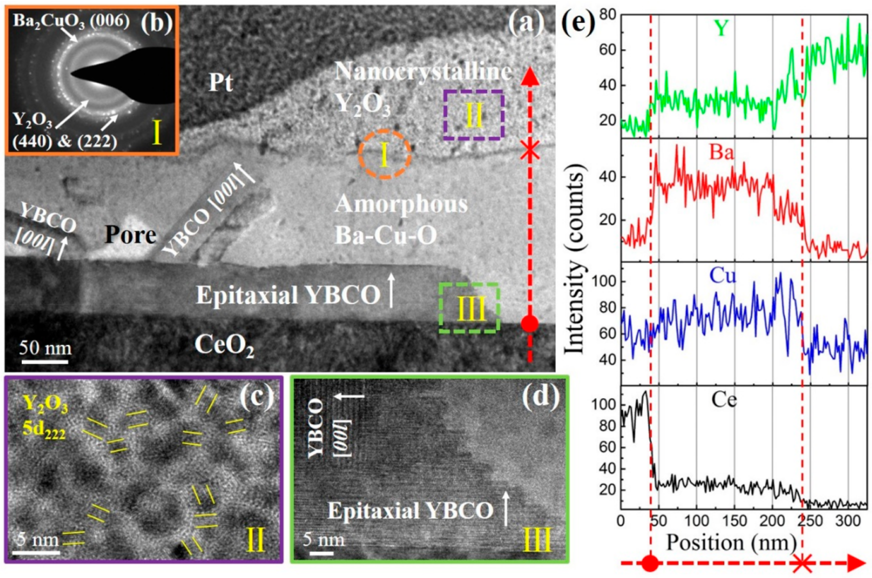

Figure 9. (a) HRTEM image of a YBCO film quenched at the first stage. (b) SAED pattern of the high-land area at the frame I (orange) in (a). (c) Zoom-in of the nanocrystalline region at the frame II (violet) in (a) and the signaled domain exhibits a five times Y$_2$O$_3$ $d_{(222)}$ spacing. (d) Zoom-in of the region of YBCO growth front within the frame III (green) in (a). (e) EDS line scans along the vertical dash line (thickness direction) for Y, Ba, Cu, and Ce.

microstructure characteristics are included. Two main clusters of Raman spectra are identified corresponding to these different topographical areas. Both these two spectra clearly exhibit a Raman shift at 336 cm^{-1} and ~466 cm^{-1} but with slight intensity differences. These two peaks concern, respectively, the vibration modes of oxygen of the CuO$_2$ planes (O$_2$−O$_3$ out-of-phase) and into apical sites (O$_4$) of orthorhombic YBCO.[41,42] Their positions and their reciprocal intensity ratios are consistent with a mixture of *a*- and *c*-axis orientations. In addition, residual traces of Ba−Cu−O phases are observed but hardly saying exact composition, since their signature phonons overlap with the broad scattering centered near 600 cm^{-1}.[43] It indicates that although there are significant differences in morphology, the phase composition and the growth orientation of YBCO are similar.

In the high-land areas (as shown in Figure 8a,b), a thin YBCO layer with 30 nm height and a sharp interface are observed. This suggests that epitaxial YBCO grains nucleate on the CeO$_2$ layer, and no interface reaction takes place in the nucleation stage due to the relatively short dwell time. Besides the epitaxial grains, YBCO crystals with other orientations were also observed in the film body. Some are in conjunction with the epitaxial grains, while some are isolated. This is consistent with the XRD results discussed in section 3.2; i.e., presence of broad YBCO (103) diffraction ring and weak YBCO (200) and (00*l*) spots. Coexistence of polycrystalline and epitaxial grains reveal that the body nucleation is still inevitable and competes with interface nucleation even under large undercooling conditions (high temperature and rapid ramping rate). Other than the YBCO phase, we also observed nanosized Y$_2$O$_3$ crystals along YBCO grain boundaries (Figure 8c, zoom-in region on the YBCO growth front at the frame I in Figure 8b).

In the low-lying area (Figure 8d), a trapezoid-shaped grain with 60 nm height forms at the interface, while it seems that this grain was not able to completely cover the substrate. Compared with the thinner epitaxial YBCO layer in Figure 8a,b, the thick and large epitaxial grain appearing in the low-lying area is evidence of the proceeding of YBCO conversion reaction. Moreover, a large width-height ratio (i.e., a width of 700 nm and a height of 60 nm) confirmed that the growth rate of the YBCO *a*/*b* plane is higher than that of the *c*-axis direction due to the high anisotropy.[44] A set of sharp diffraction spots in SAED (Figure 8e) confirms that it is indeed a well-crystallized grain with rotated-cube orientation with respect to the CeO$_2$ underneath (i.e., [100] (00l) YBCO // [110] (00l) CeO$_2$). By carefully checking the diffraction pattern in the area III (Figure 8f), we notice that weak spots corresponding to YBCO phase show up, which indicates that a very thin epitaxial YBCO layer forms at the interface as well. Two individual nucleation sites at this local region imply that the nucleation and growth process in the FF-MOD route is governed by the Volmer−Weber heteroepitaxial mode. This is because the CeO$_2$ substrate contains a mix of different terminations primarily due to roughness caused by grain boundaries and surface disturbance caused by dislocations. Therefore, the volume energy of a nucleus dominates the surface energy in the case of a low contact angle value.[16]

In order to further illustrate the nucleation process, we focused on the region including a low-lying and a high-land area with clear boundaries (Figure 9a). The height difference between these two areas is about 100 nm, which is consistent with the AFM results. Some inclined YBCO grains appear above the trapezoid-shaped YBCO grain, while some irregular-shaped pores (bright regions) are trapped in the film body. The latter is associated with the CO$_2$ gas released from the Ba−Cu−O conversion reaction. Besides this, the sidestep shaped growth front (Figure 9d) connects with the amorphous Ba−Cu−O, which is a sign of spiral growth mode of the FF-MOD YBCO film. Similar growth modes have also been reported in other in situ growth techniques, e.g., CVD[45] and PLD,[46] and screw dislocations are related to these growth features; especially, they could act as intrinsic pinning centers. Interestingly, we have noticed two distinct microstructures with a clear boundary in the high-land area which is indicative of the significant composition difference between the upper and lower parts (i.e., area I in Figure 9a). Combining the high magnification image (Figure 9c) and SAED analysis (Figure 9b), it is known that the high-land area mainly contains polycrystalline nanosized Y_2O_3 (ICSD 43-1036) and Ba_2CuO_3 (ICSD 44-0404). Besides these two nanocrystals, there are also other amorphous phases. However, the exact phase composition is hardly identified due to the complexity of the Ba−Cu−O phases. EDS (Figure 9e) was carried out in order to understand the elemental distribution along the thickness direction in the high-land area. It was found that Y, Ba, and Cu appeared simultaneously above the CeO_2 interface (noted as solid red dot). At the upper-lower region boundary (noted as red cross), the content of Y tends to increase, while the content of Ba and Cu decreases accordingly. Figure 9c presents a zoom-in image, where ordered domains with the characteristic *d*(222) spacing of the Y_2O_3 phase embed in the amorphous matrix. It suggests that phase separation (i.e., Y_2O_3 precipitates from Ba−Cu−O phase) already occurs prior to the strong *c*-axis orientation nucleation process. With elevating the sintering temperature, Y_2O_3 starts to dissolve into Ba−Cu−O to form YBCO. As the reaction proceeds, the YBCO nuclei grow rapidly in some regions, thus resulting in the coexistence of the low-lying area and the high-land areas.

From the TEM analysis, we found that the final and intermediate phases coexist in one specimen. Moreover, on the basis of the XRD results (Figure 5d), we determined the existence of polycrystalline and epitaxial YBCO grains, especially polycrystalline ones, are dominant. It is reasonable for the existence of the intermediate phase (i.e., Y_2O_3 and Ba−Cu−O), which is also consistent with the reaction path reported previously.[20] The YBCO conversion mechanism based on the solid-state reaction is clear; i.e., $BaCO_3$ first reacts with CuO to generate the $BaCuO_2$ phase, followed by a further reaction with CuO to form an enhanced transient liquid phase. YBCO eventually forms through the reaction of the liquid phase and Y_2O_3.[20] However, we did not observe the $BaCO_3$ phase due to the specimen quenched from the high sintering temperature, which tells us that most of $BaCO_3$ has already reacted with CuO and thus is consistent with the observed irregular-shaped holes. In addition, in the highland area, the composition segregation along the thickness direction is clearly observed. It is well-known that MOD processes normally yield atomic uniformity of composition in the precursor film. Therefore, the nonuniform microstructure here is related to the sintering, which is an important clue for deeply understanding the mechanism of YBCO nucleation and growth especially for the FF-MOD process. It is supposed that Ba−Cu−O is liquid phase at high temperature, while Y_2O_3 with a highly stable phase is solid. Therefore, at high sintering temperatures, Y_2O_3 with lower density (5.03 g/cm^3) compared with Ba−Cu−O, (e.g., 6.28 g/cm^3 of Ba_2CuO_3) tends to diffuse toward the film surface, thus leading to the Y segregation compared to Ba and Cu. However, one should bear in mind that segregation of Y_2O_3 and Y_2O_3 redissolution to form YBCO occurs simultaneously without obvious boundaries due to the high heating rate. In addition, the specimen quenched at this condition was highly heterogeneous; i.e., different regions underwent different reaction stages in the specimen, and the degree of Y_2O_3 segregation might vary.

Considering the fact that TEM analysis only characterizes local structures, SIMS which provides more statistical information was also engaged. Depth profiles of each composition were analyzed by SIMS on a fully reacted YBCO film, in order to confirm the distribution of elements in the thickness direction. In Figure 10, we observed that three main elements, Y, Ba, and Cu show different trends along the thickness. From 100 to 250 nm thickness, the distribution of Ba and Cu is relatively uniform; i.e., there is no obvious segregation along the thickness direction. However, when approaching to the film surface (i.e., from 0 nm of 100 nm), the content of Y increases slightly compared with Ba and Cu, which is consistent with the result of the intermediate reaction shown in the EDS-TEM study. It suggests that although most of the Y_2O_3 is consumed by the YBCO conversion reaction, still a small amount of it remains even after the full reaction with a long dwell time. This is highly in agreement with the previous SEM and TEM observation of a YBCO film grown on the single crystal.[24] Combining with the TEM analysis, we summarize that the Y_2O_3 phase first undergoes the segregation from the Ba−Cu−O matrix, which is related to the $BaCO_3$ and CuO reaction and formation of the heavy liquid phase. Afterward, it dissolves into Ba−Cu−O during the YBCO formation. Interestingly, at the CeO_2 interface, a sharp decrease of Y and Cu is clearly observed, but the content of Ba reduced smoothly. It is related to the fluctuation of the elements and interface reaction; i.e., a small amount of $BaCeO_3$ still forms at the interface, but with a weak signal hardly being detected by XRD.

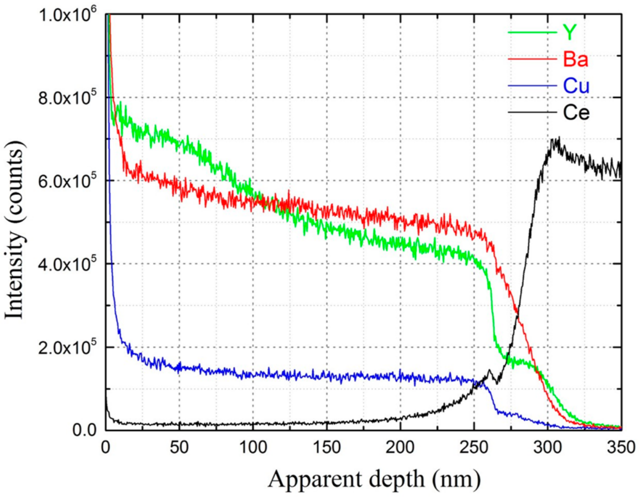

Figure 10. SIMS spectra along the thickness direction on a fully reacted YBCO film (sintered at optimized conditions).

On the basis of the aforementioned results and discussion, the nucleation, growth, and over-reacted processes of a YBCO film deposited on the CeO_2 substrate by using the FF-MOD method are proposed in the shape of model as illustrated in Figure 11, which mainly includes the following phases. First, a precursor with uniform distribution of Y_2O_3, $BaCO_3$, and CuO nanograins forms after decomposition process, as shown in Figure 11a. This stage is a result of the volatilization of the organic solvent and the decomposition of the metal organic salts at the low heat treatment temperature (below 500 °C in our case). Obviously, it is independent of the substrate and is similar to the decomposition behaviors as in form of powder. Second, with elevating the sintering temperature, the interface and body nucleation compete with each other as displayed in Figure 11b. $BaCO_3$ reacts with CuO, thus converting to Ba−

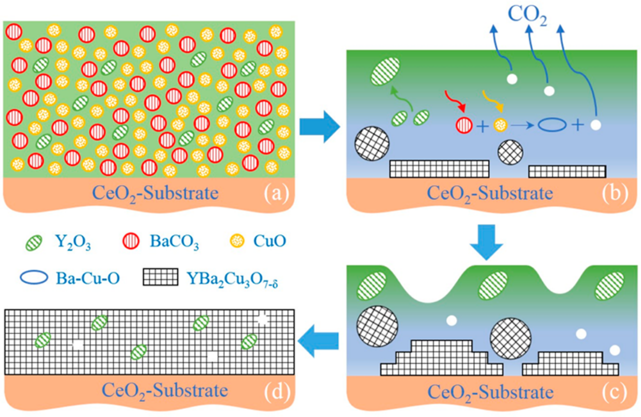

Figure 11. Schematic of the YBCO nucleation and growth on CeO_2 technical substrate by using the FF-MOD process.

Cu−O phases with the release of CO_2 according to reaction eqs 3 and 4. Meanwhile, the nanocrystalline Y_2O_3 undergoes the segregation to the film surface and then dissolves into Ba−Cu−O during the YBCO formation, as suggested by eq 5. These reaction pathways are consistent with those reported previously.[20]

$$BaCO_3 + CuO \rightarrow BaCuO_2 + CO_2(g)\uparrow \tag{3}$$

$$BaCuO_2 + CuO \rightarrow \text{liquid}\ (Ba - Cu - O) + xO_2(g)\uparrow \tag{4}$$

$$\frac{1}{2}Y_2O_3(s) + \text{liquid}\ (Ba - Cu - O) \rightarrow YBa_2Cu_3O_{7-\delta}(s) + yO_2(g)\uparrow \tag{5}$$

At the interface, YBCO epitaxially nucleates by following the Volmer−Weber growth mode; i.e., individual islands first form at preferred nucleation sites on the CeO_2 substrate, and then the polycrystalline grains nucleate in the film body due to the sufficient large Gibbs energy barrier. Third, nuclei at the interface have a significant growth advantage over those in the body. As the epitaxial YBCO grains grow faster in the lateral direction, the film shows different microstructures characteristics but similar element and phase composition, i.e., low-lying and high-land areas, as displayed in Figure 11c. However, the low-lying area corresponds to an advanced stage of the epitaxial growth process, whereas the high-land area lags behind, which is also supported by the large thickness reduction at the low-lying areas. As a result, the YBCO (103) peak intensity gradually decreases, while the YBCO (006) peak becomes stronger. So this stage is mainly dominated by the key heat treatment parameters, such as growth temperature, dwell time, and pO_2. The fourth step in our model is the further growth of epitaxial grains. At this stage, the individual epitaxial grains rapidly grow and coalesce by consuming polycrystalline grains and intermediate phases, which leads to a dense YBCO film continuously covering the entire substrate surface, as shown in Figure 11d. Meanwhile, the YBCO grains with secondary orientations almost disappear. Finally, the well-orientated YBCO layer is formed, while the unreacted Y_2O_3 present inside and the pores leave by gas release. The fifth and the final step is the over-reaction (not shown in the model), where the well-oriented YBCO layer reacts with the CeO_2 layer, thus leading to the decomposition of YBCO to $BaCeO_3$, CuO_x, and Y-211 (Y_2BaCuO_5), as described in eq 6. Thus, the quality of the YBCO film degrades with the increasing amount of $BaCeO_3$.

$$YBa_2Cu_3O_{7-\delta}(\text{ textured}) + CeO_2 \rightarrow BaCeO_3 + CuO_x + Y_2BaCuO_5 + zO_2(g)\uparrow \tag{6}$$

4. CONCLUSIONS

In this work, the influence of the sintering temperature, dwell time, and pO_2 on the microstructure of the YBCO film deposited on the CeO_2 technical substrates by using a FF-MOD method was investigated. By establishing a kinetic phase diagram of YBCO film growth, it is found that it undergoes four representative stages of nucleation, growth, and interfacial reaction over time during the overall sintering process. On the basis of this, a complete nucleation and growth model was illustrated. First, the interface nucleation and body nucleation compete with each other. Second, nuclei at the interface have a significant growth advantage over those in the body. Third, the individual epitaxial grains rapidly grow and coalesce by consuming polycrystalline grains and intermediate phase. Fourthly, the well-orientated YBCO layer further reacts with the CeO_2 layer at the interface which leads to the decomposition of YBCO. Under the optimal process conditions, a J_c value of 3.6 MA/cm^2 at 77 K self-field is achieved on a YBCO film, while the J_c (θ, H) behavior is improved compared to that on the single crystal, which is mainly attributed to a certain amount of uncorrelated defects, such as the high density of short stacking faults, Y_2O_3 nanoprecipitations, pores from gas release, etc. This work improves the understanding of the nucleation and growth mechanism of superconducting film on CeO_2-buffered technical substrates and also provides the guidance for the improvement of the superconducting performance of YBCO.

■ AUTHOR INFORMATION

Corresponding Author

*E-mail: yuezhao@sjtu.edu.cn. Tel: 0086-21-50817399. Fax: 0086-21-5441-5519.

ORCID

Jingyuan Chu: 0000-0001-6312-0593
Yue Zhao: 0000-0002-7231-2156
Mukarram Z. Khan: 0000-0001-6903-2308

Notes

The authors declare no competing financial interest.

■ ACKNOWLEDGMENTS

The authors would like to acknowledge the financial support from National Natural Science Foundation of China (Grant No. 51502171), Instrument Analysis Center of Shanghai Jiao Tong University for performing RISE and PPMS, and Center for Advanced Electronic Materials and Devices (AEMD) for performing SEM.

■ REFERENCES

(1) Larbalestier, D.; Gurevich, A.; Feldmann, D. M.; Polyanskii, A. High-T_c superconducting materials for electric power applications. *Nature* **2010**, *414*, 311−320.

(2) Weiss, J. D.; Mulder, T.; ten Kate, H. J.; van der Laan, D. C. Introduction of CORC wires: highly flexible, round high-temperature superconducting wires for magnet and power transmission applications. *Supercond. Sci. Technol.* **2017**, *30*, 014002−9.

(3) Hahn, S.; Kim, K.; Kim, K.; Hu, X.; Painter, T.; Dixon, I.; Kim, S.; Bhattarai, K. R.; Noguchi, S.; Jaroszynski, J.; Larbalestier, D. 45.5-T direct-current magnetic field generated with a high-temperature superconducting magnet. *Nature* **2019**, *570*, 496−499.

(4) Queraltó, A.; de la Mata, M.; Arbiol, J.; Obradors, X.; Puig, T. Disentangling epitaxial growth mechanisms of solution derived functional oxide thin films. *Adv. Mater. Interfaces* **2016**, *3*, 1600392−12.

(5) Araki, T.; Hirabayashi, I. Review of a chemical approach to $YBa_2Cu_3O_{7-x}$-coated superconductors-metalorganic deposition using trifluoroacetates. *Supercond. Sci. Technol.* **2003**, *16*, R71−R94.

(6) Solovyov, V.; Dimitrov, I. K.; Li, Q. Growth of thick $YBa_2Cu_3O_7$ layers via a barium fluoride process. *Supercond. Sci. Technol.* **2012**, *26*, 0130011−19.

(7) Geohegan, D. B. Physics and diagnostics of laser ablation plume propagation for high-T_c superconductor film growth. *Thin Solid Films* **1992**, *220*, 138−145.

(8) Hawley, M.; Raistrick, I. D.; Beery, J. G.; Houlton, R. J. Growth Mechanism of Sputtered Films of $YBa_2Cu_3O_7$ Studied by Scanning Tunneling Microscopy. *Science* **1991**, *251*, 1587−1589.

(9) Norton, D. P. Science and technology of high-temperature superconducting films. *Annu. Rev. Mater. Sci.* **1998**, *28*, 299−347.

(10) Feldmann, D. M.; Holesinger, T. G.; Cantoni, C.; Feenstra, R.; Nelson, N. A.; Larbalestier, D. C.; Verebelyi, D. T.; Li, X.; Rupich, M. Grain orientations and grain boundary networks of $YBa_2Cu_3O_{7-\delta}$ films deposited by metalorganic and pulsed laser deposition on biaxially textured Ni-W substrates. *J. Mater. Res.* **2006**, *21*, 923−934.

(11) Feldmann, D. M.; Larbalestier, D. C.; Holesinger, T.; Feenstra, R.; Gapud, A. A.; Specht, E. D. Evidence for Extensive Grain Boundary Meander and Overgrowth of Substrate Grain Boundaries in High Critical Current Density ex Situ $YBa_2Cu_3O_{7-x}$ Coated Conductors. *J. Mater. Res.* **2005**, *20*, 2012−2020.

(12) Obradors, X.; Puig, T.; Ricart, S.; Coll, M.; Gazquez, J.; Palau, A.; Granados, X. Growth, nanostructure and vortex pinning in superconducting $YBa_2Cu_3O_7$ thin films based on trifluoroacetate solutions. *Supercond. Sci. Technol.* **2012**, *25*, 123001−32.

(13) Schwartz, R. W.; Schneller, T.; Waser, R. Chemical solution deposition of electronic oxide films. *C. R. Chim.* **2004**, *7*, 433−461.

(14) Rupich, M. W.; Li, X.; Thieme, C.; Sathyamurthy, S.; Fleshler, S.; Tucker, D.; Thompson, E.; Schreiber, J.; Lynch, J.; Buczek, D.; DeMoranville, K.; Inch, J.; Cedrone, P.; Slack, J. Advances in second generation high temperature superconducting wire manufacturing and R&D at American Superconductor Corporation. *Supercond. Sci. Technol.* **2010**, *23*, 014015−9.

(15) Witte, M.; Gottstein, G.; de Boer, N.; Gilges, S.; Klöwer, J.; Bäcker, M.; Brunkahl, O.; Wojtyniak, B.; Mader, W.; Svete, M.; Hühne, S.-M.; Lepper, S.; Böhm, R.; Schebera, M. The Project Supra Metall: Towards Commercial Fabrication of High-Temperature Superconducting Tapes. *Adv. Eng. Mater.* **2014**, *16*, 539−549.

(16) Solovyov, V. F.; Abraimov, D.; Miller, D.; Li, Q.; Wiesmann, H. Correlation between $YBa_2Cu_3O_7$ nuclei density and the grain orientation of the CeO_2 buffered Ni-W template of the second-generation superconducting wire. *J. Appl. Phys.* **2009**, *105*, 1139271−1139277.

(17) Holesinger, T. G.; Civale, L.; Maiorov, B.; Feldmann, D. M.; Coulter, J. Y.; Miller, D. J.; Maroni, V. A.; Chen, Z.; Larbalestier, D. C.; Feenstra, R.; Li, X.; Huang, Y.; Kodenkandath, T.; Zhang, W.; Rupich, M. W.; Malozemoff, A. P. Progress in Nanoengineered Microstructures for Tunable High-Current, High-Temperature Superconducting Wires. *Adv. Mater.* **2008**, *20*, 391−407.

(18) Matsui, H.; Tsukada, K.; Tsuchiya, T.; Sohma, M.; Yamaguchi, I.; Kumagai, T.; Manabe, T. Reduced crystallization time of YBCO in a fluorine-free MOD process using uv-lamp irradiation. *Phys. C* **2011**, *471*, 960−962.

(19) Wesolowski, D. E.; Patta, Y. R.; Cima, M. J. Conversion behavior comparison of TFA-MOD and non-fluorine solution-deposited YBCO films. *Phys. C* **2009**, *469*, 766−773.

(20) Vermeir, P.; Cardinael, I.; Schaubroeck, J.; Verbeken, K.; Backer, M.; Lommens, P.; Knaepen, W.; D'haen, J.; De Buysser, K.; Van Driessche, I. Elucidation of the Mechanism in Fluorine-Free Prepared $YBa_2Cu_3O_{7-\delta}$ Coatings. *Inorg. Chem.* **2010**, *49*, 4471−4477.

(21) Yamada, K.; Kaneko, K.; Yoshida, Y.; Nishiyama, T.; Teranishi, R.; Suzuki, K.; Ito, M.; Miura, O.; Kita, R. Influences of calcination temperature on growth and superconducting properties of $GdBa_2Cu_3O_{7-\delta}$ films fabricated by fluorine-free metal organic deposition method. *Micron* **2013**, *50*, 44−50.

(22) Zhao, Y.; Chu, J.-Y.; Qureishy, T.; Wu, W.; Zhang, Z.-W.; Mikheenko, P.; Johansen, T. H.; Grivel, J.-C. Structural and superconducting characteristics of $YBa_2Cu_3O_7$ films grown by fluorine-free metal-organic deposition route. *Acta Mater.* **2018**, *144*, 844−852.

(23) Chu, J.-Y.; Zhao, Y.; Ji, Y.-T.; Wu, W.; Shi, J.-T.; Hong, Z.-Y.; Ma, L.; Suo, H.-L.; Jin, Z.-J. Interface reaction-governed hetero-epitaxial growth of $YBa_2Cu_3O_{7-\delta}$ film on CeO_2-buffered technical substrate. *J. Am. Ceram. Soc.* **2019**, *102*, 5705−5715.

(24) Zhao, Y.; Torres, P.; Tang, X.; Norby, P.; Grivel, J.-C. Growth of Highly Epitaxial $YBa_2Cu_3O_{7-\delta}$ Films from a Simple Propionate-Based Solution. *Inorg. Chem.* **2015**, *54*, 10232−10238.

(25) Zhao, Y.; Zhu, J.-M.; Jiang, G.-Y.; Chen, C.-S.; Wu, W.; Zhang, Z.-W.; Chen, S.-K.; Hong, Y.- M.; Hong, Z.-Y.; Jin, Z.-J.; Yamada, Y. Progress in fabrication of second generation high temperature superconducting tape at Shanghai Superconductor Technology. *Supercond. Sci. Technol.* **2019**, *32*, 044004−6.

(26) Jiruse, J.; Hanicinec, M.; Havelka, M.; Hollricher, O.; Ibach, W.; Spizig, P. Integrating focused ion beam-scanning electron microscope with confocal Raman microscope into a single instrument. *J. Vac. Sci. Technol., B: Nanotechnol. Microelectron.: Mater., Process., Meas., Phenom.* **2014**, *32*, 06FC03−6.

(27) Wiesinger, H. P.; Sauerzopf, F. M.; Weber, H. W. On the calculation of J_c from magnetization measurements on superconductors. *Phys. C* **1992**, *203*, 121−128.

(28) Khan, M.Z.; Malmivirta, M.; Zhao, Y.; Wu, X.; Jha, R.; Awana, V.P.S.; Huhtinen, H.; Paturi, P. Angular and field dependent flux pinning in artificially doped YBCO films on IBAD-MgO based template. *Phys. C* **2018**, *555*, 15−23.

(29) Zhao, Y.; Tang, X.; Wu, W.; Grivel, J.-C. Influence of Substrate-Film Reactions on YBCO Grown by Fluorine-Free MOD Route. *IEEE Trans. Appl. Supercond.* **2017**, *27*, 1−4.

(30) Ovchinnikov, Y. N.; Ivlev, B. I. Pinning in layered inhomogeneous superconductors. *Phys. Rev. B: Condens. Matter Mater. Phys.* **1991**, *43*, 8024−8029.

(31) Kim, S. I.; Gurevich, A.; Song, X.; Li, X.; Zhang, W.; Kodenkandath, T.; Rupich, M. W.; Holesinger, T. G.; Larbalestier, D. C. Mechanisms of weak thickness dependence of the critical current density in strong-pinning ex situ metal-organic-deposition-route $YBa_2Cu_3O_{7-x}$ coated conductors. *Supercond. Sci. Technol.* **2006**, *19*, 968−979.

(32) Civale, L.; Maiorov, B.; MacManus-Driscoll, J. L.; Wang, H.; Holesinger, T. G.; Foltyn, S. R.; Serquis, A.; Arendt, P. N. Identification of intrinsic ab-plane pinning in YBa/sub 2/Cu/sub 3/O/sub 7/ thin films and coated conductors. *IEEE Trans. Appl. Supercond.* **2005**, *15*, 2808−2811.

(33) Civale, L.; Maiorov, B.; Serquis, A.; Willis, J. O.; Coulter, J. Y.; Wang, H.; Jia, Q. X.; Arendt, P. N.; MacManus-Driscoll, J. L.; Maley, M. P.; Foltyn, S. R. Angular-dependent vortex pinning mechanisms in $YBa_2Cu_3O_7$ coated conductors and thin films. *Appl. Phys. Lett.* **2004**, *84*, 2121−2123.

(34) Palau, A.; Durrell, J. H.; MacManus-Driscoll, J. L.; Harrington, S.; Puig, T.; Sandiumenge, F.; Obradors, X.; Blamire, M. G. Crossover between Channeling and Pinning at Twin Boundaries in $YBa_2Cu_3O_7$ Thin Films. *Phys. Rev. Lett.* **2006**, *97*, 2570021−4.

(35) Blatter, G.; Geshkenbein, V. B.; Larkin, A. I. From isotropic to anisotropic superconductors: A scaling approach. *Phys. Rev. Lett.* **1992**, *68*, 875−878.

(36) Puig, T.; Gutiérrez, J.; Pomar, A.; Llordés, A.; Gázquez, J.; Ricart, S.; Sandiumenge, F.; Obradors, X. Vortex pinning in chemical solution nanostructured YBCO films. *Supercond. Sci. Technol.* **2008**, *21*, 034008−12.

(37) Xu, A.; Jaroszynski, J.; Kametani, F.; Larbalestier, D. Broad temperature range study of J_c and H_{irr} anisotropy in $YBa_2Cu_3O_x$ thin films containing either Y_2O_3 nanoparticles or stacking faults. *Appl. Phys. Lett.* **2015**, *106*, 0526031−0526035.

(38) Ohnishi, T.; Huh, J. U.; Hammond, R. H.; Jo, W. High Rate in situ $YBa_2Cu_3O_7$ Film Growth Assisted by Liquid Phase. *J. Mater. Res.* **2004**, *19*, 977−981.

(39) Bhuiyan, M. S.; Paranthaman, M.; Salama, K. Solution-derived textured oxide thin films—a review. *Supercond. Sci. Technol.* **2006**, *19*, R1−R12.

(40) Vermeir, P.; Feys, J.; Schaubroeck, J.; Verbeken, K.; Lommens, P.; Van Driessche, I. Influence of sintering conditions in the preparation of acetate-based fluorine-free CSD YBCO films using a direct sintering method. *Mater. Res. Bull.* **2012**, *47*, 4376−4382.

(41) Iliev, M.; Zhang, P.; Habermeier, H.-U.; Cardona, M. Raman spectroscopy as analytical tool for the local structure of $YBa_2Cu_3O_x$ thin films. *J. Alloys Compd.* **1997**, *251*, 99−102.

(42) Camerlingo, C.; Delfino, I.; Lepore, M. Micro-Raman spectroscopy on YBCO films during heat treatment. *Supercond. Sci. Technol.* **2002**, *15*, 1606−1609.

(43) Chen, Z.; Maroni, V. A.; Miller, D. J.; Li, X.; Rupich, M. W.; Feenstra, R. Examination of through-thickness/through-time phase evolution during an MOD-type REBCO precursor conversion using Raman microscopy. *Supercond. Sci. Technol.* **2010**, *23*, 085006−9.

(44) Puig, T.; González, J. C.; Pomar, A.; Mestres, N.; Castaño, O.; Coll, M.; Gázquez, J.; Sandiumenge, F.; Piñol, S.; Obradors, X. The influence of growth conditions on the microstructure and critical currents of TFA-MOD $YBa_2Cu_3O_7$ films. *Supercond. Sci. Technol.* **2005**, *18*, 1141−1150.

(45) Ma, Y.; Watanabe, K.; Awaji, S.; Motokawa, M. Observation of growth-mode change under a magnetic field in$YBa_2Cu_3O_{7-x}$. *Phys. Rev. B: Condens. Matter Mater. Phys.* **2002**, *65*, 1745281−5.

(46) Marré, D.; Diaspro, A.; Ferdeghini, C.; Grassano, G.; Pallecchi, I.; Siri, A. Two-dimensional growth of atomically smooth YBCO epitaxial films deposited by PLD in a pulsed oxygen flow. *Supercond. Sci. Technol.* **1998**, *11*, 737−743.